33RD CONGRESS
OF THE INTERNATIONAL COUNCIL
OF THE AERONAUTICAL SCIENCES
STOCKHOLM, SWEDEN, 4-9 SEPTEMBER, 2022

ICAS 2022 SWEDEN

ACCURATE TWO-DIMENSIONAL STEADY-STATES FOR THE SUPERSONIC FLOW OVER A COMPRESSION CORNER

Ricardo Santos[1], Leonardo Alves[1], Nicolas Cerulus[2], Helio Quintanilha Jr.[2] & Vassilios Theofilis[2,3]

[1]Universidade Federal Fluminense, Brazil
[2]University of Liverpool, UK
[3]Universidade de São Paulo, Brazil

Abstract

The present paper describes the numerical issues that had to be overcome in order to generate of accurate steady-states for the supersonic flow over a compression corner. Low and high-order shock capturing schemes for spatial discretization coupled with a nonlinearly stable explicit marching scheme for time integration were employed to do so. The flow parameters considered in this study include a Mach number of $M = 3$ and a ramp angle of $\theta = 10^o$, for different Reynolds numbers based on the leading edge to corner length, namely $Re = 2 \times 10^3$, 5×10^3, 10×10^3 and 20×10^3. Grid convergence studies indicate the existence of an apparent grid convergence in space, which is associated with only a few orders of magnitude residue decay in time. When employing low-order schemes, a severe grid refinement is required as the Reynolds number increases in order to eventually obtain a residue decay in time towards machine precision. Such a Reynolds related grid refinement constraint can be severely minimized by employing high-order schemes. This issue appears to be caused by the reattachment shock. Since the resulting two-dimensional steady-state is linearly (modally and non-modally) stable for this Mach number, ramp angle and Reynolds numbers, this lack of residue convergence in time is likely due to numerical issues caused by poor spatial convergence.

Keywords: Spatial grid convergence, residue decay in time, false convergence, linear and modal stability

1. Introduction

Experimental studies of separation observed in shock / boundary-layer interaction (SBLI) problems for different geometrical variations from the classical flat plate were first performed more than half a century ago [1, 2]. Separation is one of the key phenomena associated with the laminar-turbulence transition in high speed flows. The same can be said about its stable/unstable dynamics. Both are very important for the identification of the laminar / transitional / turbulent regions in such supersonic and hypersonic external flows. This is the very reason why SBLI problems are still the subject of intensive studies today [3, 4]. In the present paper, focus is placed on the supersonic flow over a compression corner, which is illustrated in Fig. 1.

A few classical early studies are worth mentioning here. Carter used a first-order predictor-corrector scheme for time integration and a second-order finite-difference scheme for spatial discretization to obtain steady-states with (Mach,Reynolds) number pairs equal to $(M, Re) = (3, 1.68 \times 10^4)$, $(4, 6.8 \times 10^4)$ and $(6.06, 1.5 \times 10^5)$, with the latter based on the leading edge to corner length, using ramp angles of $\theta = 5^o$, 7.5^o and 10^o [5]. Many relevant characteristics of these flows were quantified, such as incipient separation and bubble size, showing good agreement with experimental data [6]. Hung and MacCormack used the second-order accurate, in both time and space, two-step MacCormack scheme to simulate this problem with $M = 14.1$, $Re = 1.04 \times 10^5$ and $\theta = 15^o$, 18^o and 24^o [7] and validate their pressure and skin friction coefficient results against experimental data [8]. They also compared velocity profiles with inviscid theory and numerical simulations [5], showing some important differences with respect to the former and good agreement with the latter. These two-dimensional

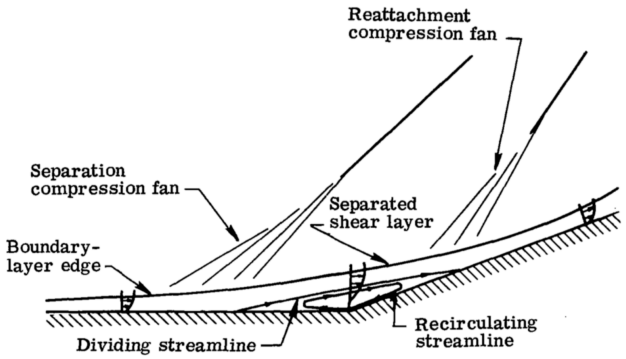

Figure 1 – Illustration of the compression corner studied in this paper [5].

simulations were replicated and extended to three dimensions by Rudy *et al.*, who compared the performance of four different finite-difference and finite-volume based solvers [9]. All these studies solved the compressible Navier-Stokes equations, prescribing all variables at the inflow boundary and extrapolating all variables at the outflow boundary.

Only very recent studies are now described in more detail, since most of the earlier ones have already been reviewed elsewhere [3, 4]. Chuvakhov *et al.* obtained two and three-dimensional steady-states using the HSFlow solver, based on a quasi-monotonic Godunov-type scheme that is second-order accurate in both time and space, for a compression corner with $M = 8$, $Re = 3.71 \times 10^5$ and $\theta = 15^o$ [10]. The latter simulations modeled the effect of small bluntness elements at the leading edge, which lead to the appearance of the stationary Görtler vortices observed in their own experimental data. Sidharth *et al.* obtained two-dimensional steady-states using US3D, under an implicit Euler marching of a second-order spatial discretization based on a modified Steger-warming fluxes using MUSCL limiters, for a double corner with $M = 5$, $Re = 6.8 \times 10^5$ and $\theta = 12 - 20^o$ [11]. It was used in a bi-global linear and modal stability analysis, which identified an unstable stationary mode. This implied the existence of a three-dimensional steady-state, which was confirmed by their three-dimensional US3D simulations. Dwivedi *et al.* extended these tools to include a resolvent analysis [12], applying them to the aforementioned compression corner [10]. This allowed them to verify that the steady and three-dimensional reattachment streaks previously attributed to a centrifugal instability were in fact caused by baroclinic effects. They also verified that the streak spanwise wavelength was selected by the perturbations present in both separation bubble and reattaching shear layer. Hao *et al.* obtained two-dimensional steady-states using the PHAROS solver, which uses an implicit line relaxation for time integration of a second-order spatial discretization based on a modified Steger-Warming scheme, for a compression corner with $M = 7.7$, $Re = 4.2 \times 10^5$ and several ramp angles between $\theta = 11^o$ and 15^o [13]. A bi-global linear stability analysis revealed the existence of stationary modes at both small and large spanwise wavelengths, but oscillatory modes were only found at the former. Recirculation bubble size and disturbance amplitudes increased when increasing ramp angle and decreasing wall temperature. These results were verified by unsteady three-dimensional simulations using a third-order explicit strong-stability-preserving scheme to march in time a higher-order spatial discretization based on a fifth-order WENO scheme for inviscid fluxes and a sixth-order central-difference scheme for the viscous fluxes [14]. Exposito *et al.* used the same aforementioned US3D solver to evaluate both blunt leading edge and finite span effects on three-dimensional steady-states with $M = 9.66$, $Re = 1.07 \times 10^5$ as well as $\theta = 10^o$ and 20^o [15], comparing it with triple deck theory. The separation region increased when increasing bluntness. Furthermore, three-dimensional effects were confined to the side edges, which appears to have prevented the appearance of secondary vortices.

The above review suggests that steady-states for the compression corner problem illustrated in Fig. 1 are obtained using at most second-order schemes in the spatial discretization. Hence, the goal of the present paper is to discuss the numerical issues associated with obtaining such steady-states using high-order schemes in both time and space instead. It is important to note that only two-dimensional steady-states are presented and discussed here.

2. Mathematical Model

The governing equations simulated in this work are the unsteady and two-dimensional Navier-Stokes equations for the conservative variables and written under a generalized coordinate framework. All fluid properties are assume constant, expect the dynamic viscosity, which follows Sutherland's law. The fluid is also assumed to behave as an ideal gas with a constant Prandtl number. Furthermore, an undisturbed free-stream is assumed to reach the sharp leading edge of the flat and horizontal plate that is upstream of the compression corner. Finally, this plate can either be adiabatic or have a constant temperature.

3. Numerical Method

An in-house code is employed here to solve these governing equations. Called 3D4S, it has been under development over the past few years and some preliminary results have been published [16, 17, 18, 19]. Inviscid flux discretization uses either the Roe flux-difference splitting [20] coupled with a second-order TVD scheme with an entropy fix [21, 22] or the Lax-Friedrichs flux splitting coupled with one of many characteristic-wise fifth-order WENO schemes [23, 24, 25, 26, 27]. The latter WENO scheme is employed here, since it was tailored for steady-states. Viscous flux discretization uses the classical conservative central-difference schemes with either second, fourth or sixth-order. The second one is used here to enhance numerical stability. 3D4S can perform steady-state simulations using dual-time-stepping [28] with an implicit Euler scheme as well as multi-step [29] and multi-stage [30] MGM schemes. It can perform time-accurate unsteady simulations as well, using either second, third or fourth-order strong-stability-preserving explicit Runge-Kutta schemes [31]. Implicit as well as explicit versions are parallelized with a distributed memory framework. The third-order explicit solver is used here, since two-dimensional compression corner steady-states are likely asymptotically stable to two-dimensional disturbances in a linear, modal and global sense.

Finally, it is important to note that a structured grid is employed, since 3D4S uses finite difference schemes applied on generalized coordinates. It is obtained from an elliptic grid generation procedure that solves a Poisson-type equation, which allows grid clustering control as well as orthogonality enforcing at pre-defined boundaries [32]. This equation is discretized with second-order central-difference schemes, where same order biased schemes are applied at the boundaries. The resulting nonlinear system os algebraic equations is solved using Gauss-Seidel iteration coupled with the Successive Over-Relaxation Method. It is important to note that convergence rates of this iterative solver usually decrease as the number of boundaries where orthogonality is enforced increases.

4. Results

The compression corner simulations presented here consider a Mach number of $M = 3$, a corner angle of $\theta = 10^o$ and several Reynolds numbers between $Re = 10^4$ and 3×10^5. Pressure, density and temperature free stream conditions are, respectively, $p_\infty = 101325\,Pa$, $\rho_\infty = 1.17661\,kg/m^3$ and $T_\infty = 300\,K$. The two coefficient Sutherland's law defines the dynamic viscosity, i.e. $\mu = c_s T^{3/2}/(T + T_s)$ with $T_s = 383.54\,K$ and $c_s = 1.458 \times 10^{-6}\,kg/(m\,s\,K^{1/2})$. Furthermore, the specific heat at constant pressure and the Prandtl number are fixed at $C_{P_\infty} = 1005\,J/(kg\,K)$ and $Pr = 0.72$, which connects the thermal conductivity k to Sutherland's law.

4.1 Low-Order Scheme

Before any results can be analyzed, it is important to verify spatial grid convergence. This is done for both low and high-order schemes. Low-order here means the second-order TVD scheme for inviscid fluxes and the second-order central schemes for viscous fluxes. High-order, on the other hand, means the fifth-order steady-state tailored WENO scheme for inviscid fluxes and the fourth-order central scheme for viscous fluxes. One example of such an analysis is shown in Fig. 2, where the results were obtained using the low-order scheme with a prescribed wall temperature of $T_W = 300\,K$. It presents the density (left) and vertical velocity (right) profiles in the wall normal direction measured at the corner for different Reynolds number, namely $Re = 2 \times 10^3$ (top), $Re = 5 \times 10^3$ (middle) and $Re = 10 \times 10^3$ (bottom). As the number of grid points in the stream wise, i.e. N_X, and wall normal, i.e. N_Y, directions increase, these low-order results for both density and vertical velocity profiles appear

to spatially grid converge for approximately $(N_X, N_Y) = (3601, 1201)$, $(4201, 1401)$ and $(4801, 1601)$, respectively. Both Euclidean and maximum residue convergence in time towards machine precision in the former case, which represents approximately 10 orders of magnitude. However, only 2 to 3 orders of magnitude convergence in time is observed for these residues in the latter case. Hence, the solution obtained for $Re = 10 \times 10^3$ is not a disturbance free steady-state. It is instead a steady-state disturbed by undamped temporal content. One should note that the middle case residue convergence in time behaves like the latter (former) for the two smaller (four larger) grid sizes.

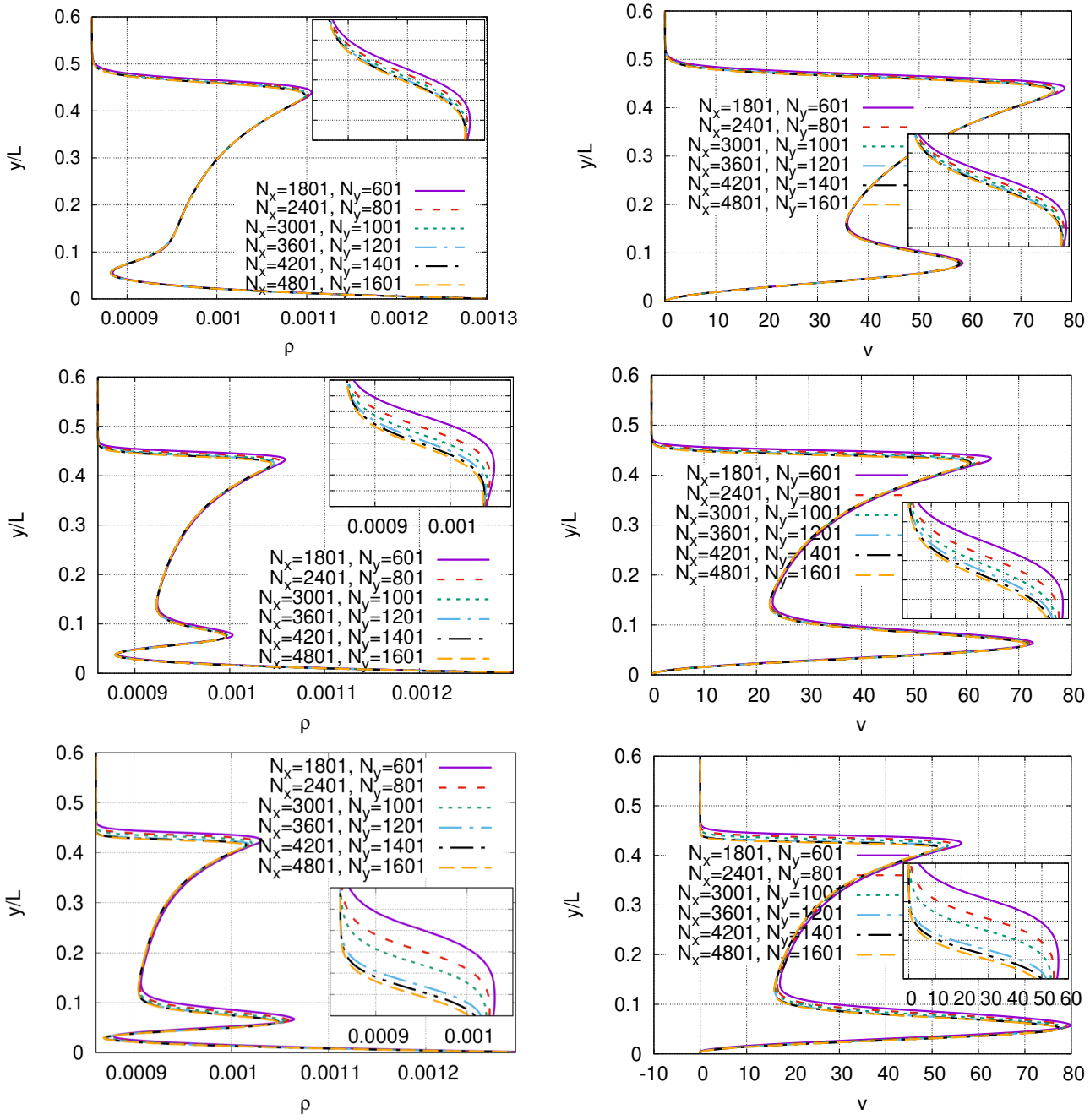

Figure 2 – Low-order scheme results for a prescribed temperature of $T_W = 300\,K$ showing density (left) and vertical velocity (right) profiles in the wall normal direction measured at the corner at different Reynolds numbers $Re = 2 \times 10^3$ (top), $Re = 5 \times 10^3$ (middle) and $Re = 10 \times 10^3$ (bottom).

Density and vertical velocity isocontours for the particular case with a prescribed temperature of $T_W = 300\,K$ and a Reynolds number of $Re = 10^4$ obtained with $(N_X, N_Y) = (4801, 1601)$ are shown in Fig. 3. Their respective residue has only converged 2 to 3 orders of magnitude in time. It should be noted that the bubble size is small at this Reynolds number, so separation and reattachment shocks are not clearly distinguishable from each other.

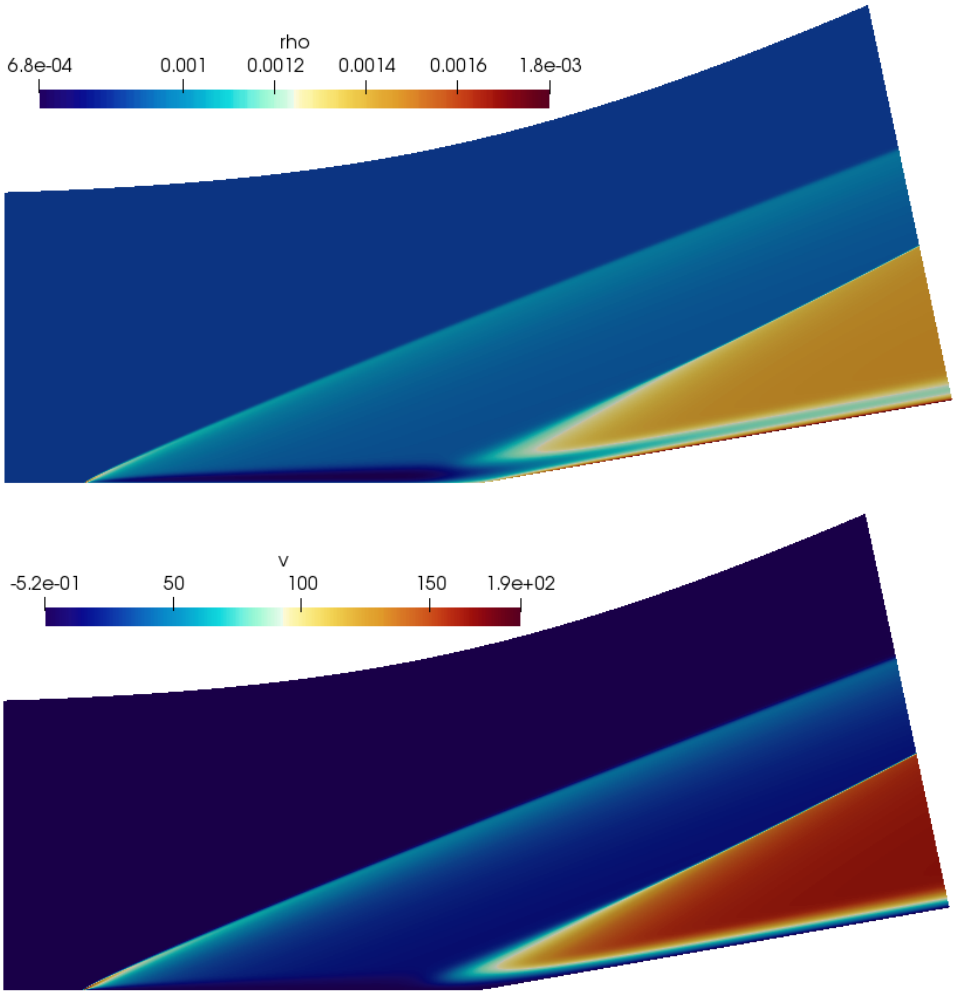

Figure 3 – Low-order scheme results obtained with $(N_X, N_Y) = (4801, 1601)$ for a prescribed temperature of $T_W = 300\,K$ and Reynolds numbers of $Re = 10^4$ are shown for the density (top) and vertical velocity (bottom) isocontours.

Reynolds numbers typically studied in the relevant literature, however, are significantly larger. This presents a serious difficulty for simulations using low-order spatial schemes, since increasingly larger grid sizes are required to generate disturbance free two-dimensional steady-states as the Reynolds number increases. Disturbance free in the present scenario means the spatial grid is refined enough to allow the residue to converge in time as well. Similar compression corner simulations performed with second-order schemes found in the literature have used $(N_X, N_Y) = (900, 300)$ [10], $(525, 200)$ [11], $(577, 349)$ [12] and $(1600, 600)$ [13]. Such grid sizes are all smaller than the ones used here even though their respective studies considered significantly higher Reynolds numbers than the ones considered here. However, none of these studies provided such residue convergence histories.

4.2 High-Order Scheme

One alternative to minimize these issues is to use high-order schemes instead. For this reason, another example of a grid convergence analysis is shown in Fig. 4, but now for the high-order scheme with an adiabatic wall and a Reynolds number of $Re = 20 \times 10^3$. It presents the same type of data shown in Fig. 2. In this case, however, density grid convergence is observed at $(N_X, N_Y) = (1801, 601)$. Once again, the maximum density residue temporal behavior confirms this observation, which is qualitatively similar to the one observed in the middle case of Fig. 2. Only a two orders of magnitude residue decay in time is achieved for the two smaller grids, but this number changes to ten orders of magnitude for the larger grid. These results indicate that high-order schemes are necessary for grid convergence because of the computational cost reduction they provide by allowing an appropriate residue decay in time to be obtained for much smaller grids.

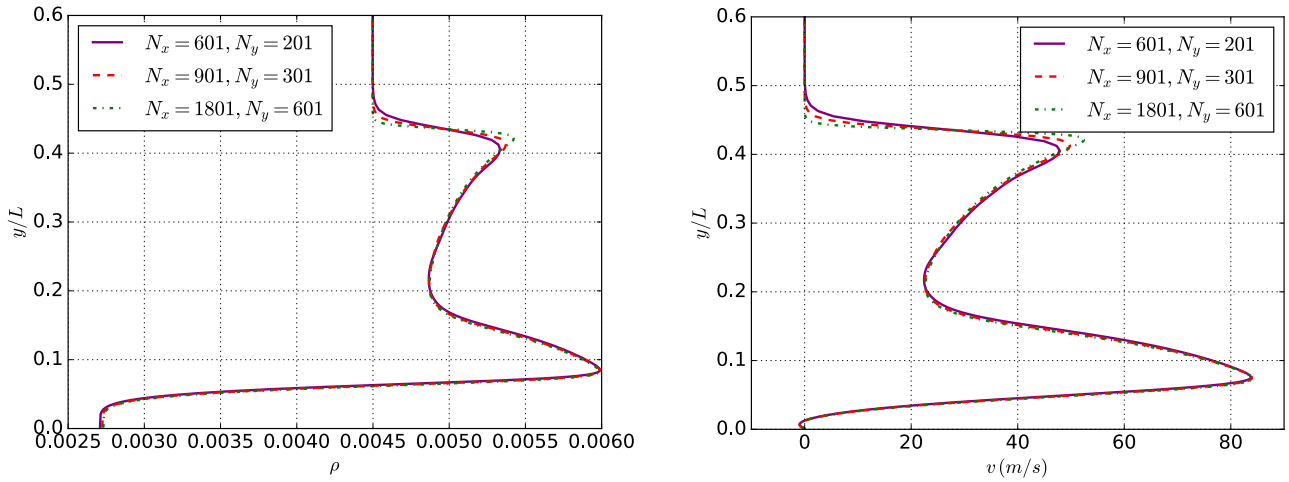

Figure 4 – Same as Fig. 2, but for the high-order scheme with $Re = 20 \times 10^3$ and an adiabatic wall.

Finally, density and vertical velocity isocontours for the particular case with an adiabatic wall and a Reynolds number of $Re = 2 \times 10^4$ obtained with $(N_X, N_Y) = (1801, 601)$ are shown in Fig. 5. Their respective residue has converged approximately 10 orders of magnitude in time. Bubble size is larger at this Reynolds number, so separation and reattachment shocks can be clearly distinguished from each other. These preliminary results indicate that the reattachment shock region is responsible for the dominant errors in the residue calculation over time.

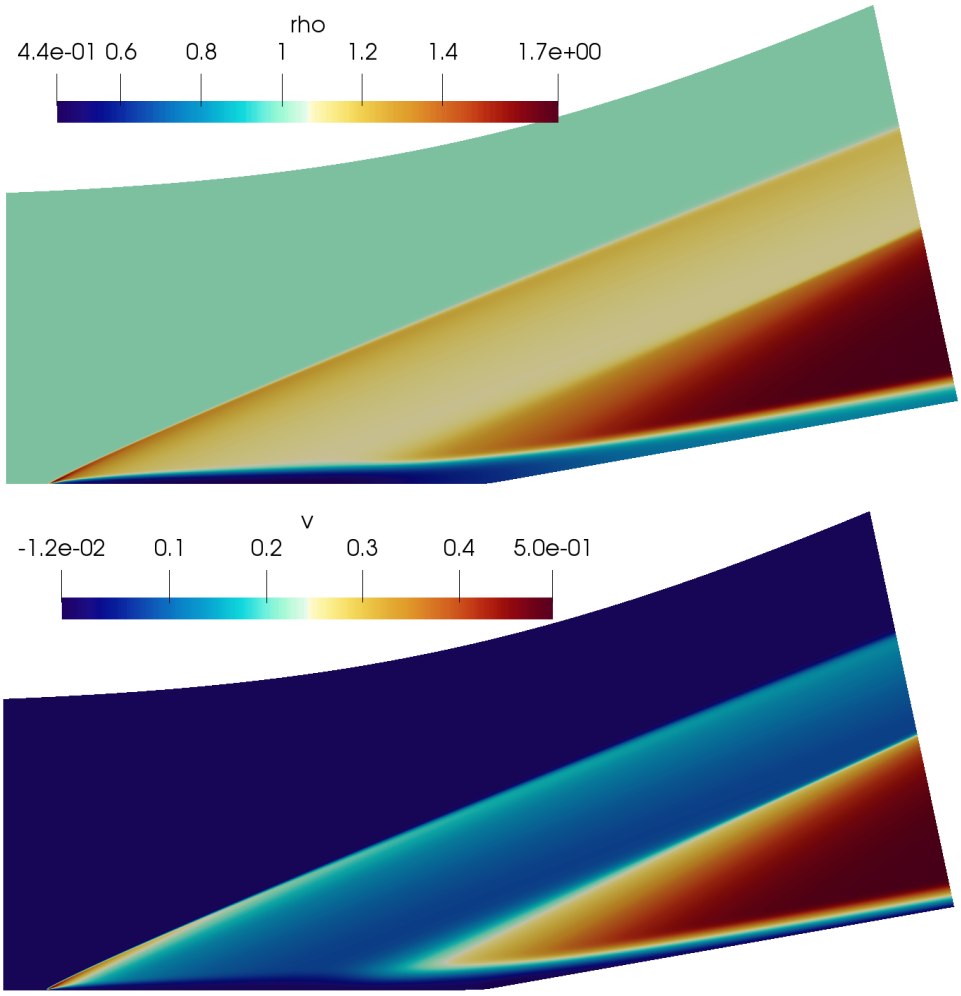

Figure 5 – Same as Fig. 3, but for the high-order scheme with $Re = 20 \times 10^3$ and an adiabatic wall.

5. Conclusions

The present paper provided results for the two-dimensional flow over a compression corner at a Mach number of $M = 3$ and a corner angle of $\theta = 10^o$ for several different Reynolds numbers. These results indicate that low-order numerical simulations require a prohibitive computational cost at small to moderate Reynolds numbers. Given these constraints, it is quite difficult to obtain steady-states free of temporal content with such solvers. Grid converged high-order numerical simulations, on the other hand, can generate such steady-states at much smaller computation costs. They are currently being used for a linear, modal and global two-dimensional stability analysis. These results will appear in a future publication by this same research group.

Acknowledgements

The authors would like to thank the financial support received from the AFOSR through grants FA9550-17-1-0115 (Theofilis) and FA9550-18-1-0419 (Alves), as well as the PhD Fellowship received from CAPES (Ricardo).

Contact Author Email Address

Corresponding author (Leonardo Alves) email: lsbalves@id.uff.br

Copyright Statement

References

[1] Chapman D R, Kuehn D M and Larson H K, Investigation of separated flows in supersonic and subsonic streams with emphasis on the effect of transition, *NACA Technical Note*, No. 3869, 1957.

[2] Chapman D R, Kuehn D M and Larson H K, Investigation of separated flows in supersonic and subsonic streams with emphasis on the effect of transition, *NACA Report*, No. 1356, 1958.

[3] Dolling D, Fifty years of shock wave / boundary-layer interaction research: what next? *AIAA Journal*, Vol. 39, No. 8, 2010.

[4] Gaitonde D V , Progress in shock wave / boundary-layer interactions, *Progress in Aerospace Sciences*, Vol. 72, pp 80-99, 2015.

[5] Carter J E, Numerical solutions of the Navier-Stokes equations for the supersonic laminar flow over a two-dimensional compression corner, *NASA Technical Report*, No. 385, 1972.

[6] Lewis J E, Kubota T and Lees L, Experimental investigation of supersonic laminar, two-dimensional boundary-layer separation in a compression corner with and without cooling. *AIAA Journal*, Vol. 6, No. 1, pp 7-14, 1968.

[7] Hung C and MacCormack R, Numerical solutions of supersonic and hypersonic laminar compression corner flows, *AIAA Journal*, Vol. 14, No. 4, pp 475-481, 1976.

[8] Holden M S and Moselle J R, Theoretical and experimental studies of the shock wave / boundary-layer interaction on compression surfaces in hypersonic flow, *CALSPAN Report*, No. AF-2410- A-I, 1969.

[9] Rudy D H, Thomas J L, Kumar A, Gnoffo P A and Chakravarthy S R, Computation of laminar hypersonic compression corner flows, *AIAA journal*, Vol. 29, No. 7, pp 1108-1113, 1991.

[10] Chuvakhov P V, Borovoy V Y, Egorov I V, Radchenko V N, Olivier H and Roghelia A, Effect of small bluntness on formation of Görtler vortices in a supersonic compression corner flow, *Journal of Applied Mechanics and Technical Physics*, Vol. 58, No. 6, pp 975-989, 2017.

[11] Sidharth G S, Dwivedi A, Candler G V and Nichols J W, Onset of three-dimensionality in supersonic flow over a slender double wedge, *Physical Review Fluids*, Vol. 3, No. 093901, 2018.

[12] Dwivedi A, Sidharth G S, Nichols J W, Candler G V and Jovanović M R, Reattachment streaks in hypersonic compression ramp flow: an input-output analysis, *Journal of Fluid Mechanics*, Vol. 880, pp 113-135, 2019.

[13] Hao J, Cao S, Wen C Y and Olivier H, Occurrence of global instability in hypersonic compression corner flow, *Journal of Fluid Mechanics*, Vol. 919, No. A4, 2021.

[14] Cao S, Hao J, Klioutchnikov I, Olivier H and Wen C Y, Unsteady effects in a hypersonic compression ramp flow with laminar separation, *Journal of Fluid Mechanics*, Vol. 912, No. A3, 2021.

[15] Exposito D, Gai S L and Neely A J, Wall temperature and bluntness effects on hypersonic laminar separation at a compression corner, *Journal of Fluid Mechanics*, Vol. 922, No. A1, 2021.

[16] Santos R D, Alves L S B, Cerulus N and Theofilis V, On two-dimensional steady-states of supersonic flows over compression ramps and their global linear instability, *AIAA SciTech Conference*, No. 2321, 2019.

[17] Santos R D and Alves L S B, Generation of Steady-States with Discontinuities using Minimal Gain Marching Schemes, *AIAA Aviation Conference*, No. 2839, 2019.

[18] Burtsev A, Quintanilha Jr. H R, Theofilis V, Santos R D and Alves L S B, Linear instability mechanisms of supersonic flow past blunt bodies, *AIAA SciTech Conference*, No. 0050, 2021.

[19] Santos R and Alves L S B, A comparative analysis of explicit, IMEX and implicit strong stability preserving Runge-Kutta schemes, *Applied Numerical Mathematics*, Vol. 159, pp 204-220, 2021.

[20] Roe P L, Approximate Riemann solvers, parameter vectors, and difference schemes. *Journal of Computational Physics*, Vol. 43, pp 357-372, 1981.

[21] Harten A, High resolution schemes for hyperbolic conservation laws, *Journal of Computational Physics*, Vol. 49, No. 3, pp 357-393, 1983.

[22] Harten A and Hyman J M, Self adjusting grid methods for one-dimensional hyperbolic conservation laws, *Journal of Computational Physics*, Vol. 50, No. 2, pp 235-269, 1983.

[23] Jiang G S and Shu C W, Efficient implementation of weighted ENO schemes, *Journal of Computational Physics*, Vol. 126, pp 202-228, 1996.

[24] Henrick A K, Aslam T D and Powers J M, Mapped weighted essentially non-oscillatory schemes: achieving optimal order near critical points. *Journal of Computational Physics*, Vol. 207, pp 542-567, 2005.

[25] Borges R B de R, Carmona M, Costa B and Don W S, An improved weighted essentially non-oscillatory scheme for hyperbolic conservation laws, *Journal of Computational Physics*, Vol. 227, No. 6, pp 3191-3211, 2008.

[26] Acker F, Borges R B, Costa B, An improved WENO-Z scheme, *Journal of Computational Physics*, Vol. 313, No. C, pp 726-753, 2016.

[27] Zhu J and Shu C W, Numerical study on the convergence to steady state solutions of a new class of high order WENO schemes, *Journal of Computational Physics*, Vol. 349, pp 80-96, 2017.

[28] Jameson A, Time dependent calculations using multigrid, with applications to unsteady flows past airfoils and wings, *AIAA CFD Conference*, No. 1596, 1991.

[29] Teixeira R S and Alves L S B, Minimal gain marching schemes: searching for unstable steady-states with unsteady solvers, *Theoretical and Computational Fluid Dynamics*, Vol. 31, No. 5, pp 607-621, 2017.

[30] Santos R D, Nunes M S S, Veloso R T and Alves L S B, Multi-stage minimal gain marching schemes as efficient steady-state solvers, *in preparation*, 2022.

[31] Gottlieb S, Ketcheson D and Shu C W, Strong stability preserving Runge-Kutta and multistep time discretizations, *Word Scientific*, 2011.

[32] Spekreijse S P, Elliptic grid generation based on Laplace equations and algebraic transformations. *Journal of Computational Physics*, Vol. 118, No. 1, pp 38-61, 1995.

[33] Theofilis V and Colonius T, An algorithm for the recovery of 2- and 3-D BiGlobal Instabilities of Compressible Flow Over 2-D Open Cavities, *AIAA Fluid Dynamics Conference and Exhibit*, No. 4143, 2003.

[34] Quintanilha Jr. H R, Paredes P, Hanifi A and Theofilis V, Transient growth analysis of hypersonic flow over an elliptic cone, *Journal of Fluid Mechanics*, Vol. 935, No. A40, 2022.